Supplemental Information

Classical Lamination Theory

Classical lamination theory (CLT) is the traditional stress analysis tools for thin fiber reinforced laminates [1]. It is common to construct the so-called ABD matrix, in order to relate mid-surface strains and curvatures to force and moment resultants (stress resultants per unit length) (Equation S1). The 6x6 ABD matrix for homogenized layers is given in Equation S2, and components of S2 are computed using S3.

$$\begin{bmatrix} M_x \\ M_y \\ M_{xy} \\ M_x \\ M_y \\ M_{xy} \end{bmatrix} = \mathbf{ABD} \cdot \begin{bmatrix} \varepsilon_x^0 \\ \varepsilon_y^0 \\ \varepsilon_{xy}^0 \\ \kappa_x^0 \\ \kappa_y^0 \\ \kappa_{xy}^0 \end{bmatrix} \tag{S1}$$

$$\mathbf{ABD} = \begin{bmatrix} A_{11} & A_{12} & A_{13} & B_{11} & B_{12} & B_{13} \\ A_{12} & A_{22} & A_{23} & B_{12} & B_{22} & B_{23} \\ A_{13} & A_{23} & A_{33} & B_{13} & B_{23} & B_{33} \\ B_{11} & B_{12} & B_{13} & D_{11} & D_{12} & D_{13} \\ B_{12} & B_{22} & B_{23} & D_{12} & D_{22} & D_{23} \\ B_{13} & B_{23} & B_{33} & D_{13} & D_{23} & D_{33} \end{bmatrix} \tag{S2}$$

$$\begin{aligned} A_{ij} &= \sum_{k=1}^{N} \bar{Q}_{ij_k}(z_k - z_{k-1}) \\ B_{ij} &= \frac{1}{2}\sum_{k=1}^{N} \bar{Q}_{ij_k}(z_k^2 - z_k^2) \\ D_{ij} &= \frac{1}{3}\sum_{k=1}^{N} \bar{Q}_{ij_k}(z_k^3 - z_k^3) \end{aligned} \tag{S3}$$

where $\bar{Q}_{ij}$ are elements of the reduced stiffness matrix, and the subscript *k* denotes a specific layer, and N is the total number of layers. The TenCate laminate material was modelled as a $[0, 90]_{4S}$ laminate, with nominal material properties $\{E_1, E_2, E_3\}$ = {26.6, 26.6, 15.4} GPa, $\{G_{12}, G_{23}, G_{31}\}$ = {2.8, 4.0, 4.0} GPa, Poisson's ratios $\{\nu_{12}, \nu_{23}, \nu_{31}\}$ = {.2, .12, .12}. The 1-2 properties were provided by the manufacturer, and the 3 properties were estimated. These material properties were used to compute the $\bar{Q}_{ij}$ matrices (details can be found [1]), and then components of the ABD matrix by Equation 3. ABD matrices for TenCate laminate thicknesses of 1.9, 2, and 3mm are given in Figure S1. ABD matrices for the overmold polymer were treated as isotropic single layers for thicknesses of 4.1 and 2.92mm.

a

$$\begin{pmatrix} 5.18542\times10^7 & 1.03708\times10^7 & 0 & 0 & 0 & 0 \\ 1.03708\times10^7 & 5.18542\times10^7 & 0 & 0 & 0 & 0 \\ 0 & 0 & 5.32\times10^6 & 0 & 0 & 0 \\ 0 & 0 & 0 & 15.5995 & 3.11989 & 0 \\ 0 & 0 & 0 & 3.11989 & 15.5995 & 0 \\ 0 & 0 & 0 & 0 & 0 & 1.60043 \end{pmatrix}$$

b

$$\begin{pmatrix} 5.45833\times10^7 & 1.09167\times10^7 & 0 & 0 & 0 & 0 \\ 1.09167\times10^7 & 5.45833\times10^7 & 0 & 0 & 0 & 0 \\ 0 & 0 & 5.6\times10^6 & 0 & 0 & 0 \\ 0 & 0 & 0 & 18.1944 & 3.63889 & 0 \\ 0 & 0 & 0 & 3.63889 & 18.1944 & 0 \\ 0 & 0 & 0 & 0 & 0 & 1.86667 \end{pmatrix}$$

c

$$\begin{pmatrix} 8.1875\times10^7 & 1.6375\times10^7 & 0 & 0 & 0 & 0 \\ 1.6375\times10^7 & 8.1875\times10^7 & 0 & 0 & 0 & 0 \\ 0 & 0 & 8.4\times10^6 & 0 & 0 & 0 \\ 0 & 0 & 0 & 61.4063 & 12.2813 & 0 \\ 0 & 0 & 0 & 12.2813 & 61.4063 & 0 \\ 0 & 0 & 0 & 0 & 0 & 6.3 \end{pmatrix}$$

d

$$\begin{pmatrix} 3.67248\times10^7 & 1.28537\times10^7 & 0 & 0 & 0 & 0 \\ 1.28537\times10^7 & 3.67248\times10^7 & 0 & 0 & 0 & 0 \\ 0 & 0 & 1.19356\times10^7 & 0 & 0 & 0 \\ 0 & 0 & 0 & 308.672 & 108.035 & 0 \\ 0 & 0 & 0 & 108.035 & 308.672 & 0 \\ 0 & 0 & 0 & 0 & 0 & 100.318 \end{pmatrix}$$

e

$$\begin{pmatrix} 2.61552\times10^7 & 9.15432\times10^6 & 0 & 0 & 0 & 0 \\ 9.15432\times10^6 & 2.61552\times10^7 & 0 & 0 & 0 & 0 \\ 0 & 0 & 8.50044\times10^6 & 0 & 0 & 0 \\ 0 & 0 & 0 & 111.505 & 39.0267 & 0 \\ 0 & 0 & 0 & 39.0267 & 111.505 & 0 \\ 0 & 0 & 0 & 0 & 0 & 36.2391 \end{pmatrix}$$

Figure S1: Computed ABD matrices for a) 1.9mm TenCate laminate, b) 2mm laminate, c) 3mm laminate, d) 4.1mm overmold, e) 2.92mm overmold.

Single Leg Bending (SLB) Specimens

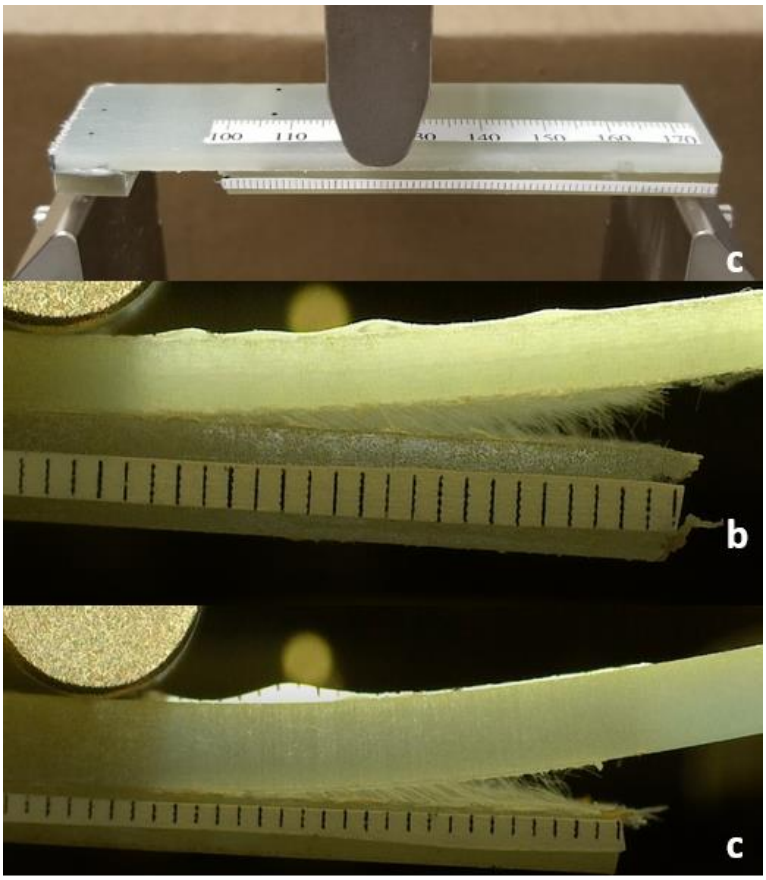

Figure S2: a) SLB specimen, modified from the ADCB geometry, loaded in 3-point bending. b) Image taken during experiment on SLB1. c) Image taken during experiment on SLB2.

The single leg bend geometry has been used to assess mixed mode fracture in various adhesive systems and between composite lamina [2-4]. In this case, the EBT model was used to assess fracture mode for the SLB specimen, in the same manner as the ADCB specimen [5]. A local approach to the fracture mode mixity analysis for the SLB specimen can be found [6]. The SLB specimens were created by removing a short segment of one arm of ADCB specimens (Figure S2a). The asymmetry of adherend thickness and material properties allows two variants of the SLB to be fabricated. Variant 1, denoted 'SLB1', had LEXAN^{TM} material removed, whereas variant 2, denoted 'SLB2', had TenCate material removed (Figure S2b, S2c). We note that the overmold materials used in the SLB tests are nominally mechanically identical to those used in ADCB tests, but have different color filler(s). Both specimens were tested in a three-point bending configuration and were monitored by a travelling optical microscope for crack length measurements. In both cases, the thickness of the TenCate beam was 3mm and the LEXAN^{TM} beam was approximately 4.1mm thick. The boundary conditions for the top beam are $N_1 = 0$, $Q_1 = P/2$, and $M_1 = (P \cdot a)/(2 \cdot B)$, and in the bottom beam section to be $N_2 = 0$, $Q_2 = -P/2$, and $M_2 = -(P \cdot a)\ )/(2 \cdot B)$, where N_i, Q_i, and M_i are axial forces, transverse forces, and moments, respectively, and P is the applied load and a the instantaneous crack length. Using the same approach presented in the analysis section, the fracture mode mixity analysis produces mode mixity angles of $\psi_{mech} = +31.8° \pm 0.1$, for SLB1 and $\psi_{mech} = -61.2° \pm 0.1$ for SLB2. When residual stress was considered, a small shift in mode mixity was produced in both specimens. $\psi_{mech+residual} = +29° \pm 0.5$, for SLB1 and $\psi_{mech+residual} = -62.7° \pm 0.3$ for

SLB2, where each component of fracture mode and mode mixity angle were computed by Equations 11-13 of the main text. Fracture energy is plotted against crack length in Figure S4 for SLB1 and SLB2, with a mean fracture energy of 1231 ± 57 for SLB1 and 2770 ± 199 for SLB2. In the case of SLB2, a fracture energy increased as a function of crack length, which could be considered rising R-curve behavior. Fiber bridging effects could possibly become more significant with increasing mode II fracture component, though too much inference should not be drawn from a single specimen (see Fig. S4).

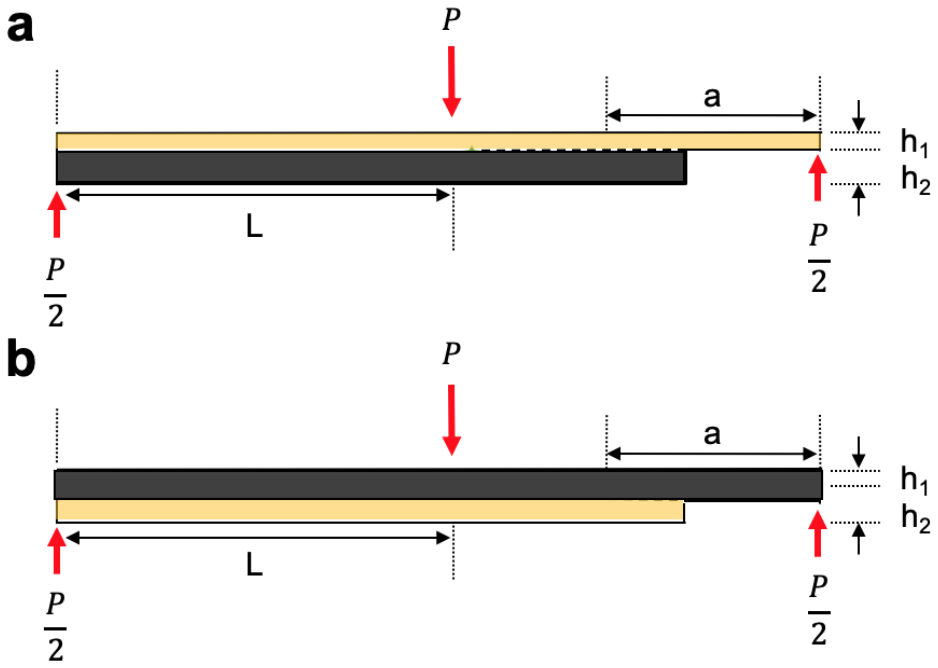

Figure S3: a) Single leg bend (SLB1) test geometry, modified from an ADCB specimen, loaded in 3-point bending. b) Complimentary SLB (SLB2) modified ADCB specimen.

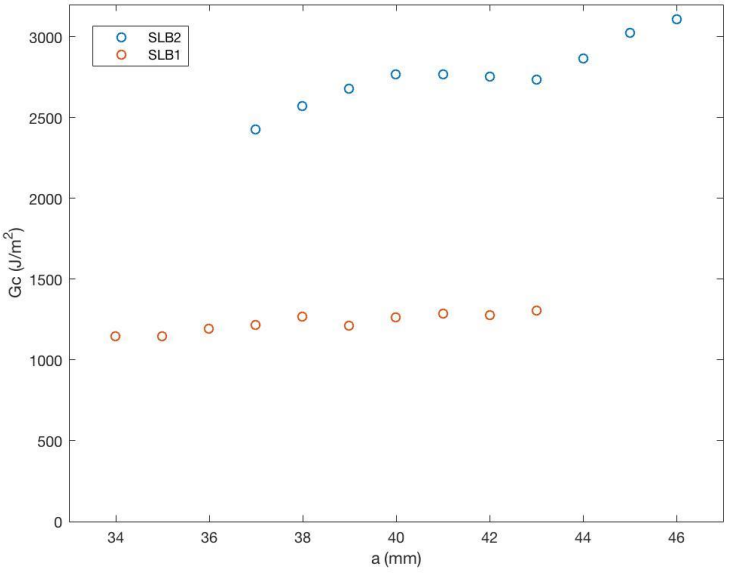

Figure S4: Critical fracture energy vs. crack length for SLB1 and SLB2.

Additional SEM Micrographs of the Fracture Surface

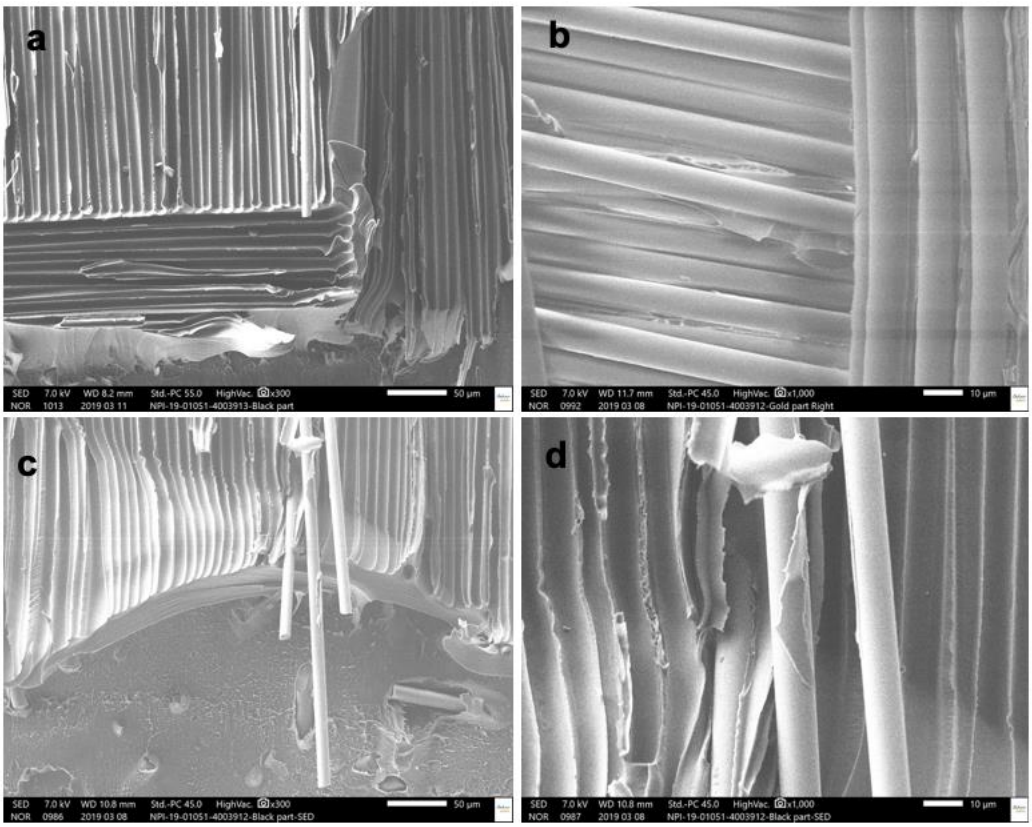

Figure S5: SEM images of the fracture surface of nominal overmold and composite fracture surface. a) Nominal overmold side of the fracture surface, however more likely the surface layer of the Tencate laminate which has bonded and transferred to the overmold material. b) Glass fiber weave pattern with some polymer showing between fiber strands. c) Transition from overmold

to surface layer of the composite laminate in the immediate vicinity of the pre-crack region. d) Close up of localized peeling of the surface sizing on glass fibers during the fracture process.

Some additional SEM images can be seen in Fig. S5 which reveal the fine structure of the fracture surface is in fact determined by the weave pattern in the fiber composite system. These images were taken at 7kV potential, under high vacuum, and the detector was tuned for the detection of emitted secondary electrons (JEOL JSM-6500F). Image magnification ranges from 50x to 1000x. In Fig. S5a, the imprinted fiber weave can clearly be seen along with a single fiber which was pulled from the weave, indicating that this is indeed the surface layer of the Tencate laminate which has bonded and transferred to the overmold material. Fig. S5b shows the glass fiber weave pattern with infiltrated polymer matrix between fiber strands. The polymer could either be a residual from the surface finish of the laminate, or it could originate from a deeper fiber and polymer layer within the laminate. In either case, the presence of fractured polymer wedged between the fibers is a positive indicator for a tough interface. In Fig. S5c, the sheath patterns on the polymer surface around fibers can be seen alongside some transferred fibers. At the bottom of the image the actual overmold interface can be seen. Fig. S5d shows a magnified view of the sheath patterns and fiber transfer. In this image a tear can be seen on the surface of the fiber, which may be the surface sizing on the glass fiber itself.

Orientation Effect

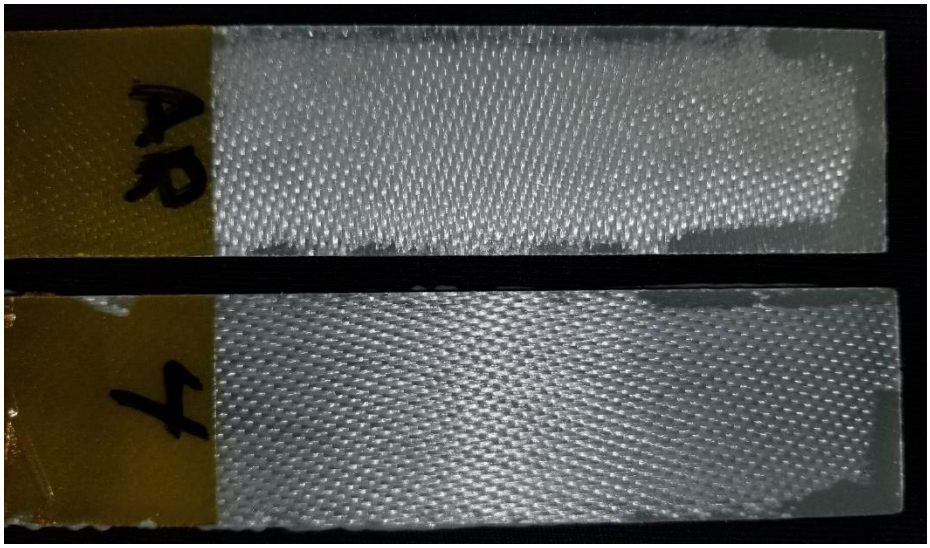

Figure S6: Change in orientation causing large increase in fracture energy. The top specimen is the non-standard orientation (G_{IC} ~ 1.8 kJ/m^2, and the bottom is standard (G_{IC} ~ 1kJ/m^2).

The unexpected results of an orientation effect on fracture energy, must be related to the fibers at the fracture surface. Most specimens were prepared so that the crack propagation direction was aligned parallel to the warp direction of the weave. However, two specimens were prepared where the crack propagation direction was parallel to the weft direction (i.e. 90° rotation of the weave pattern and perpendicular to the warp direction). Although only two specimens were tested with the alternative alignment parallel to the weft direction, both showed elevated fracture energies, nearly double those of the warp direction specimens. The discrepancy between fracture energies associated with crack propagation parallel to warp and weft directions

is certainly of interest for further characterization, and may be practically useful in industrial applications. Figure S5 shows the change in fiber orientation (top) compared to the standard orientation (bottom). It could be that the orientation of the laminate so that crack propagation occurs along the weft direction results in an intrinsic toughening effect causing a localized crack arresting effect, which would increase the energy required to propagate the crack. Some wetting issues an also be seen at the edges and ends of some specimens, which are likely a result of processing conditions which do not allow complete material flow to the edges of the ADCB mold. Processing variables that could be affecting the non-uniform interfacial bond are rate of material injection, interface temperature, an pack pressure, the details of which are worth further investigation. Bond performance was affected in these regions where falling fracture energy values are attributed to decreased bond area.

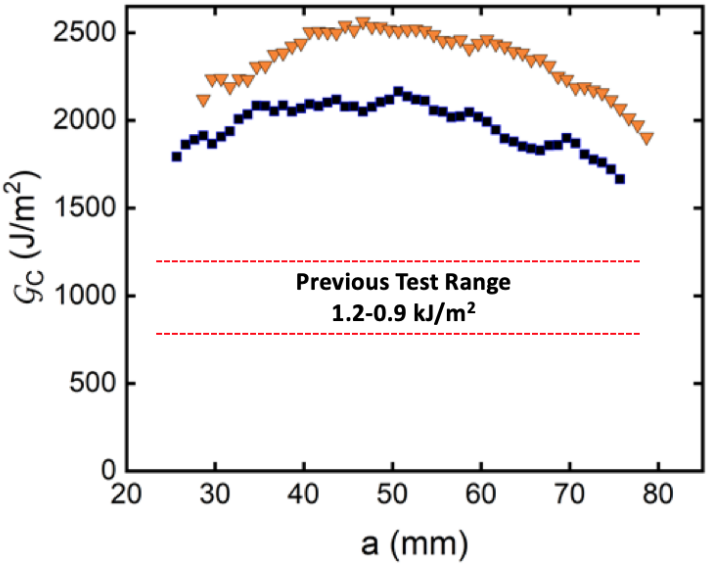

Figure S7: Weft-oriented specimens vs. warp-oriented specimens (labelled' Previous Test Range'). Falling fracture energies can be seen at increasing crack lengths, which is attributed to the reduction in bond area from lack of wetting. Initial rising behavior may be related to increasing fiber bridging, which was not observed in the warp-oriented specimens.

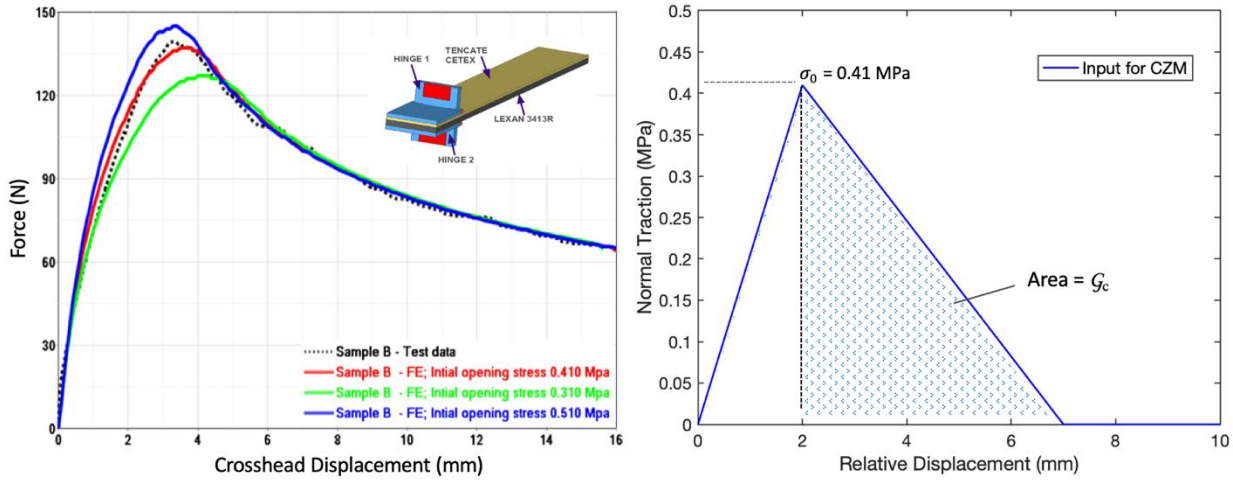

Figure S8: (left) Simulated and experimental force displacement curves. (right) Bi-linear CZM input with the key parameters of initiation stress σ_0 = .41 MPa and fracture energy of ~1kJ/m^2.

Fracture energy data is often utilized using numerical methods (i.e. finite element analysis), where stress analysis is integrated with damage evolution criteria. This approach is widely used for the simulation of damage propagation in real components, which often require more complex geometric considerations than common test geometries. Crack initiation and continuous debonding of ADCB specimens was simulated using a cohesive zone model (CZM) in the commercial finite element software package ABAQUS® [7], using a user defined element subroutine (UEL). The CZM describes material separation using cohesive surfaces with a traction-separation relation, which has been used widely to model crack propagation in DCB and related specimens under both mode I and mixed mode conditions [8, 9]. Traction-separation laws of various of forms (e.g. bi-linear, trapezoidal, exponential, etc.) may be used to approximate atomistic damage initiation and progression at the continuum scale [10-12]. Despite a variety of mathematical descriptions, the area under the traction-separation curve is equal to the critical strain energy release rate (i.e. $\mathcal{G}_c$), which is determined by experiments such as those described previously. In this work, a simple bi-linear traction-separation law was employed and only traction normal to the crack plane was considered, which is a reasonable approximation for the ADCB specimens near mode I conditions. The CZM is calibrated using the experimental ADCB data, where simulated load vs displacement curves are shown overlaid onto experimental data (Fig. S8). The calibrated damage initiation stress parameter which agrees most closely with experimental data is 0.41 MPa, and acceptable results could be achieved in the range of 0.31-0.51 MPa for the mode I specimens with critical fracture energies of ~1kJ/m^2. We note that these parameters are not physically meaningful, but rather are a function of the chosen mesh parameters (size, element type, etc) [13, 14]. Given the apparent increase in fracture energy with increasing mode mixity (Fig. 5), future efforts may include utilizing mixed mode CZM formulations that include shear sliding effects at the crack tip.

Supplemental References

[1] M. W. Hyer, *Stress analysis of fiber-reinforced composite materials*. DEStech Publications, Inc, 2009.

[2] L. Da Silva, V. Esteves, and F. J. M. u. W. Chaves, "Fracture toughness of a structural adhesive under mixed mode loadings," vol. 42, no. 5, pp. 460-470, 2011.

[3] A. Szekrényes, J. J. C. S. Uj, and Technology, "Beam and finite element analysis of quasi-unidirectional composite SLB and ELS specimens," vol. 64, no. 15, pp. 2393-2406, 2004.

[4] S. Razavi, M. Ayatollahi, E. Esmaeili, and L. J. E. J. o. M.-A. S. da Silva, "Mixed-mode fracture response of metallic fiber-reinforced epoxy adhesive," vol. 65, pp. 349-359, 2017.

[5] S. Bennati, M. Colleluori, D. Corigliano, P. S. J. C. S. Valvo, and Technology, "An enhanced beam-theory model of the asymmetric double cantilever beam (ADCB) test for composite laminates," vol. 69, no. 11-12, pp. 1735-1745, 2009.

[6] B. Davidson and V. J. I. J. o. F. Sundararaman, "A single leg bending test for interfacial fracture toughness determination," vol. 78, no. 2, pp. 193-210, 1996.

[7] A. Documentation and U. Manual, "Version 6.10," *Dassault systemes,* 2010.

[8] S. Jain, S. R. Na, K. M. Liechti, and R. T. Bonnecaze, "A cohesive zone model and scaling analysis for mixed-mode interfacial fracture," *International Journal of Solids and Structures,* vol. 129, pp. 167-176, 2017.

[9] C. Tsai, Y. Guan, D. Ohanehi, J. Dillard, D. Dillard, and R. Batra, "Analysis of cohesive failure in adhesively bonded joints with the SSPH meshless method," *International Journal of Adhesion and Adhesives,* vol. 51, pp. 67-80, 2014.

[10] R. D. Campilho, M. D. Banea, J. Neto, and L. F. da Silva, "Modelling adhesive joints with cohesive zone models: effect of the cohesive law shape of the adhesive layer," *International Journal of Adhesion and Adhesives,* vol. 44, pp. 48-56, 2013.

[11] J. Remmers, R. de Borst, and A. Needleman, "A cohesive segments method for the simulation of crack growth," *Computational mechanics,* vol. 31, no. 1-2, pp. 69-77, 2003.

[12] G. I. Barenblatt, "The mathematical theory of equilibrium cracks in brittle fracture," in *Advances in applied mechanics*, vol. 7: Elsevier, 1962, pp. 55-129.

[13] X. Lu, M. Ridha, B. Chen, V. Tan, and T. Tay, "On cohesive element parameters and delamination modelling," *Engineering Fracture Mechanics,* vol. 206, pp. 278-296, 2019.

[14] A. Turon, C. G. Davila, P. P. Camanho, and J. Costa, "An engineering solution for mesh size effects in the simulation of delamination using cohesive zone models," *Engineering fracture mechanics,* vol. 74, no. 10, pp. 1665-1682, 2007.